ARTICLE   OPEN

Preparation of epitaxial hexagonal YMnO₃ thin films and observation of ferroelectric vortex domains

Hongzhuang Pang[1], Fengyuan Zhang[1], Min Zeng[1,2], Xingsen Gao[1], Minghui Qin[1], Xubing Lu[1], Jinwei Gao[1], Jiyan Dai[3] and Qiliang Li[2]

Ferroelectric vortex is one of unique domain structures in the hexagonal $RMnO_3$ (R = Sc, Y, Ho-Lu) systems. This vortex pattern is quite sensitive to crystal imperfections, such as lattice defects and oxygen vacancies, which has been previously observed and studied in a single-crystal structure. Here we report epitaxial growth of hexagonal YMnO₃ thin films on platinum-coated Al₂O₃ (0001) substrates. High-quality epitaxial YMnO₃(0001)/Pt(111)/Al₂O₃(0001) heterostructures with sharp interfaces have been achieved and characterised by using X-ray diffractometry and transmission electron microscopy. Reversible ferroelectric domain structures have been achieved and observed with well-established piezoresponse hysteresis. Furthermore, the ferroelectric vortex domain patterns with a typical size of ~20 nm have been observed, representing a significant progress in the fabrication and exploration of topological vortices in hexagonal $RMnO_3$ thin films.

INTRODUCTION

Hexagonal rare-earth manganites (h-$RMnO_3$, R = Sc, Y, Ho-Lu) have been found to exhibit improper ferroelectricity, antiferromagnetism and novel topological vortex domain structures.[1–3] Among these manganites, hexagonal YMnO₃ (h-YMO) is one of the well-studied multiferroic materials with the coexistence of ferroelectricity (T_c ~ 1,000 K) and antiferromagnetism (T_N ~ 90 K).[4] Its ferroelectric polarisation is originated from the periodic tilting of MnO_5^{3+} polyhedral and displacements of Y^{3+} ions along a line in parallel with the c axis. As a result, one-third upward displacements and two-third downward displacements of the Y^{3+} ions along the [001] direction lead to a net electric polarisation along the c axis.[4–6] In comparison, the antiferromagnetic properties are related with the Mn^{3+}–Mn^{3+} spin interactions.

It is quite interesting that the tilting of MnO_5^{3+} polyhedral induces a trimerisation of Mn^{3+} ions in each Mn layer. This trimerisation results in a unique crystallographic domain pattern that consists of six domains with the [α⁺, γ⁻, β⁺, α⁻, γ⁺, β⁻] configuration. This is so-called the sixfold vortex domain pattern with one conjunct point.[6–10] Chae et al.[8] pointed out that this vortex pattern is in fact related with a kind of topological defects with which the structural and antiphase domain walls are interlocked with each other, leading to various intriguing phenomena, such as vortex walls, structural translation walls and antiferromagnetic walls. Currently, the topological vortex domain structures in h-YMO and its similar partners h-$RMnO_3$ have been extensively reported.[11–20] For examples, Choi et al.[11] reported the insulating interlocked ferroelectric and structural antiphase domain walls in h-YMO by conductive atomic force microscopy. Geng et al.[12] reported a direct visualisation of the coupling between the magnetic and electric vortex domains in h-ErMnO₃ by piezoresponse and magnetic force microscopy. Yu et al.[13] and Zang et al.[14] reported a direct observation of multiferroic vortex domains in h-YMO at atomic scale using the aberration-corrected scanning transmission electron microscopy (TEM). Also, the topologically vortex structures and mutual-domain coupling in h-YMO were studied by using first-principles density functional theory.[21–24]

However, the vortex domain structures have so far been observed only in bulk single crystals. There is not any clear observation of domain structure in the film, although some works have been done on the preparation of h-YMO films.[25–30] In addition, the size of vortex domain reported is quite large, in the range of several micrometres.[11–14] It will be very interesting if one can reduce the size of vortex domain because this will lead to new insights on such a unique vortex domain. Indeed, the vortex is a topologically protected defect,[8,11] different with other lattice defects, such as dislocations that will break the topological symmetry. Therefore, observation of vortex domains in thin films is difficult due to the relatively high density of defects in thin films with respect to single crystals. This poses a big challenge on the preparation of high-quality thin films, which accommodate the vortex domain structure.

This work is to meet the challenge and address the above-mentioned issues. The missions are to prepare high-quality epitaxial h-YMO thin films, and characterise the thin-film ferroelectric properties and domain structure. For hexagonal thin films such as h-YMO films, one of the difficulties to achieve epitaxy is the absence of proper bottom electrode. In this work, we first successfully prepared highly epitaxial h-YMO/Pt/Al₂O₃(0001) heterostructures. Then, we performed a series of electrical characterisations and domain observation to measure the ferroelectric performance and possible vortex domain pattern of the as-prepared thin films. The measurement included out-of-plane domain structure and local domain switching behaviours. The vortex domains were identified by using TEM.

RESULTS

Before the YMO film growth, the X-ray diffraction (XRD) θ–2θ scan was performed on Pt/ALO(0001) samples to evaluate the epitaxy of the Pt layer, as shown in Figure 1a. The Laue oscillations around the Pt(111) reflection are clearly found, indicating the good single-crystal-like film quality.[29] The XRD θ–2θ scan of the YMO/Pt/ALO (0001) heterostructure is presented in Figure 1b. Apart from the Pt (111) and Al_2O_3 (0001) (ALO(0001)) peaks, all of the observed peaks are indexed properly to the (000l) planes of h-YMO, confirming a phase-pure h-YMO film with the c axis normal to the film surface. It is suggested that the as-prepared heterostructures are of quite high crystalline quality with YMO(0001)/Pt(111)/ALO (0001) out-of-plane texture. It should be mentioned that the Laue fringes around the Pt(111) reflection is not observed in the YMO (0001)/Pt(111)/ALO(0001) heterostructures, indicating that the Pt layer quality is degraded slightly due to the thermal interruption during the subsequent deposition of YMO at 800 °C.[30]

To confirm the epitaxy of the heterostructures, we performed the ψ-scan of the (11$\bar{2}$1)-plane for the YMO layer, the (113)-plane ((11$\bar{2}$1)-plane) for the Pt layer and the (11$\bar{2}$2)-plane for the ALO substrate. The probed data are displayed in Figure 1c. All the ψ-scans around these reflections show the 60° inter-spaced peaks, corresponding to the sixfold symmetry of these planes. It is worth noting that the in-plane symmetry of the Pt layer is rotated by 28.6° with respect to the ALO substrate and YMO film due to the minimum of lattice mismatch, which will be discussed below. On the basis of these XRD data, the crystal lattice parameters are calculated to be $a = b \sim 6.311$ Å and $c = 11.403$ Å for the h-YMO layer, $a \sim 3.924$ Å for the cubic Pt layer (corresponding to $a = b \sim 2.741$ Å and $c \sim 2.265$ Å in the hexagonal structure), and $a = b = 4.758$ Å and $c = 12.992$ Å for the h-ALO layer.

The in-plane epitaxial relationships between the h-YMO (0001) film and Pt(111) layer on ALO(0001) substrate can be schematically illustrated in Figure 1d. The ALO(0001) lattice presents an in-plane parameter $a = a_{ALO} \sim 4.758$ Å, whereas the in-plane parameter for h-Pt is $a = a_{h\text{-}Pt} \sim 2.741$ Å. The distance denoted by L1 corresponds to $\sqrt{3}.a_{ALO}$, matches well with the distance $3a_{h\text{-}Pt}$. In this arrangement, an in-plane rotating angle of 30° between the Pt layer and ALO substrate is set, fitting well with the ψ-scan data in Figure 1c. Meanwhile, the in-plane parameter of h-YMO layer is $a = a_{YMO} \sim 6.311$ Å. The distance denoted by L2 corresponds to $\sqrt{3}.a_{YMO}$, equals to the distance $4a_{h\text{-}Pt}$. In this situation, it also requires an in-plane rotating angle of 30° between the Pt layer and YMO film. Therefore, the corresponding in-plane epitaxial relationship should be [10$\bar{1}$0]YMO//[11$\bar{2}$]Pt//[10$\bar{1}$0]ALO. It is noted that our results on the in-plane epitaxial relationships are significantly different from earlier reported ones. For example, Marti *et al.*[29] reported an in-plane epitaxial relationship of [10$\bar{1}$0]ALO//[11$\bar{2}$]Pt and [1$\bar{1}$00]YMO//[1$\bar{1}$0]Pt. These differences can be attributed to the big lattice constant a (≈ 6.311 Å estimated from the XRD result) in our YMO films, which is larger than that of single crystals (≈ 6.136 Å) and the reported films.[28,29] The lattice difference of $\sim 2.85\%$, defined as $[a_{YMO}(\text{film}) - a_{YMO}(\text{crystal})]/a_{YMO}(\text{crystal})$, can be attributed to the deposition at a high temperature of 800 °C. It should be noted that the in-plane lattice of YMO crystal is not matched well with that of h-Pt of 2.741 Å. The mismatch is defined as $[a_{YMO}(\text{crystal}) - 2a_{h\text{-}pt}]/2a_{h\text{-}pt}$, which in this work is up to 11.89%, suggesting that the lattice arraignment can be unstable. Furthermore, high fabrication temperature can enhance the mobility of atoms and active energy of substrate surface. Thus, it is possible to obtain a stable structure with low mismatch by rotating the in-plane stacking angle and/or adjusting the in-plane
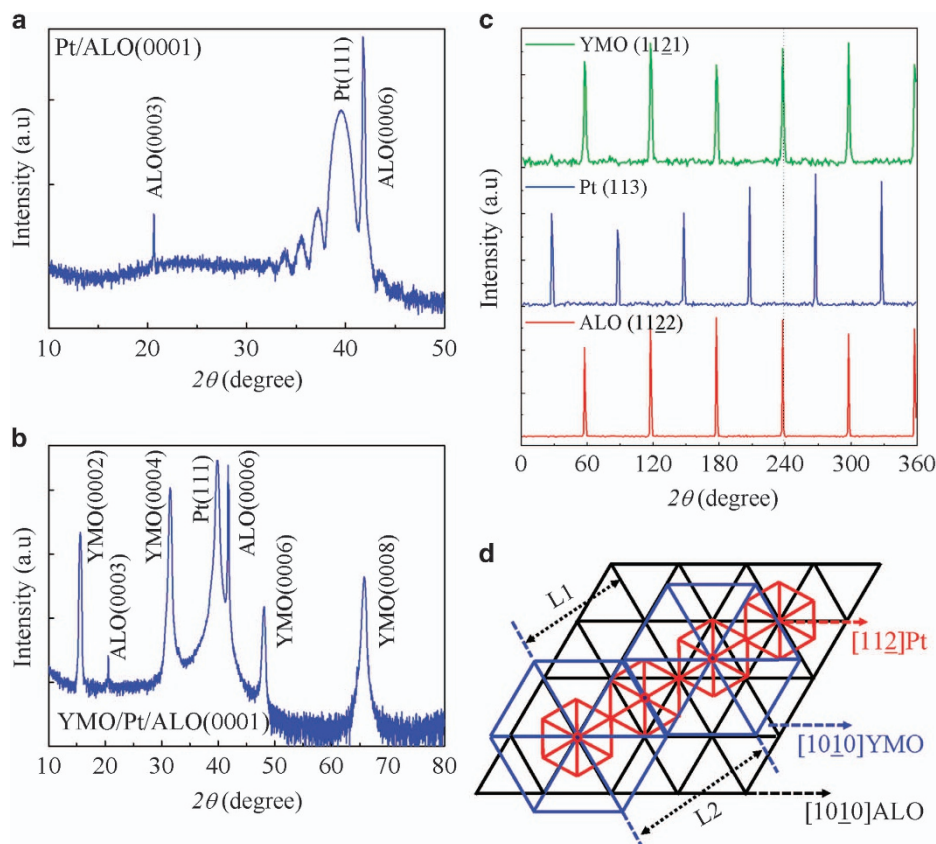

Figure 1. Epitaxial property of h-YMO film grown on Pt-coated (ALO(0001)) substrates. (**a**) XRD pattern of the Pt(111) conducting layer grown on ALO(0001) substrate. (**b**) XRD pattern of the h-YMO films grown on Pt-coated ALO(0001) substrate. (**c**) ψ-scan of h-ALO(11$\bar{2}$2), Pt(113)[h-Pt (11$\bar{2}$1)] and h-YMO(11$\bar{2}$1), and (**d**) schematic diagram of epitaxial relationship of the h-YMO films grown on Pt-coated ALO(0001) substrate.
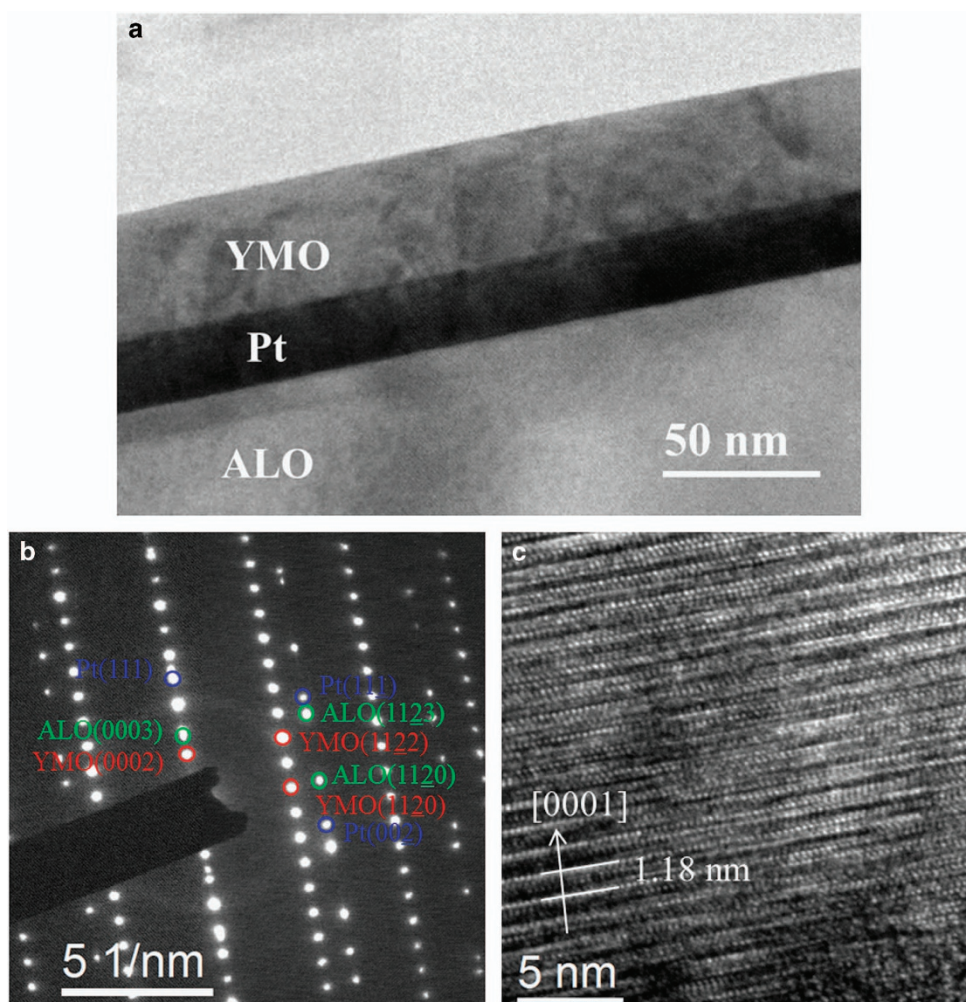
Figure 2. (a) Cross-sectional HRTEM of image showing the interface and surface among the YMO, Pt and ALO layers. (b) The selected area electron diffraction patterns of the three layers in the observed region. The circles with different colours correspond to the diffraction index of different layers. Red circles denote YMO layer, green circles denote YMO layer and blue circles denote YMO layer. (c) The higher HRTEM image of YMO layer.

lattice constant under the high fabrication temperature. After carefully analysing the lattice arrangement of YMO and Pt layer by XRD and TEM, it was found that the *a*-axis of the YMO deposited at 800 °C has a ≈30° rotation from the *a*-axis of h-Pt, which produces a tensile strain of − 3.07% [defined as $(\sqrt{3}.a_{YMO} - 4a_{h\text{-}pt})/4a_{h\text{-}pt}$]. As a result, an enlarged in-plane YMO parameter can be observed due to the tensile strain under this arraignment.

To gain better insight of the lattice quality of the hetero-structures, a cross-sectional TEM observation was performed. As shown in Figure 2a, it can be observed that both the YMO/Pt and Pt/ALO interfaces are smooth and sharp, and the YMO surface is also very flat in the imaging scale. The Pt and YMO layers are ≈22.4 and 39.2 nm in thickness, respectively. The epitaxial relationships in the imaged region were further examined by the selected area electron diffraction. The diffraction spots of the YMO, Pt and ALO layers can be well identified and clearly indexed in Figure 2b. It is noted that the out-of-plane diffraction spots of the three layers are in a straight line, indicating an excellent epitaxial property of the heterostructure. The evaluated out-of-plane lattice parameters (*c*) are 11.828, 13.056 and 2.225 Å for YMO, ALO and h-Pt, respectively. These values are in a good agreement with the results evaluated from the XRD data in Figure 1. Moreover, a high-resolution TEM (HRTEM) image of YMO layer is shown in Figure 2c. A wavy-like in-plane lattice is observed, suggesting that the

h-YMO films have two opposite polarised states, as Y and Mn atoms are dislocated in the Y–O and Mn–O layers along the [0001] direction, which are responsible for ferroelectricity observed in the films. Similar observations were reported in many previous papers.[13,14,19]

Next, the ferroelectric behaviours of the epitaxial YMO films in microscopically level were characterised using the vertical piezo-response force microscopy and typical images are summarised in Figure 3 for one sample, where the contrasts of the topography, amplitude and phase of the YMO film are shown with scanned area of $3 \times 3\,\mu m^2$. It is noted that the electric field for the amplitude and phase images is small (±3 V). It can be observed that the film surface is very flat (Figure 3a), and the surface roughness evaluated by the root-mean-square roughness is quite small ≈0.3 nm. The amplitude signals (Figure 3b) and phase signals (Figure 3c) in combination indicate the spontaneous polarisation along the *c* axis. It is noted that no clear amplitude and phase contrasts are observed, indicating the absence of spontaneous ferroelectric domains in the fresh-state YMO film. However, a higher direct current electric field with bias voltage up to ±5 V generates well-defined phase loop and piezoelectric amplitude butterfly-like loop, as shown in Figure 3d,e, respectively, demonstrating the polarisation reversal driven by the direct current bias. The present data on the epitaxial thin films evidence
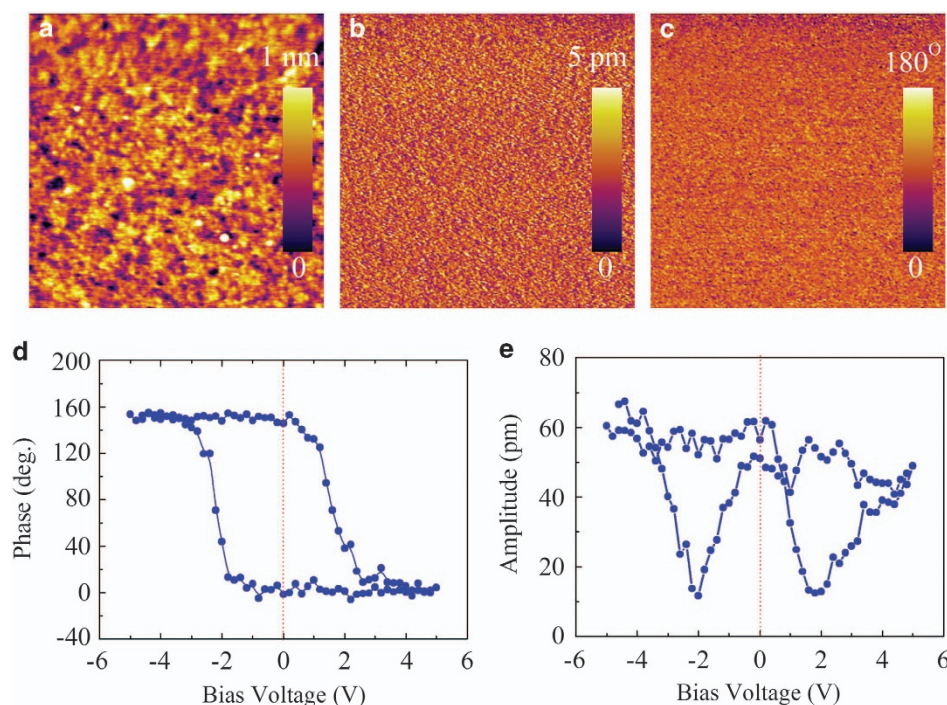
Figure 3. Piezoelectric force microscopy (PFM) image based on the *in situ* epitaxial YMO film in a $3.0 \times 3.0 \ \mu m^2$ area. (**a**) Topography (**b**) amplitude contrast, (**c**) phase contrast and local switching spectroscopy for (**d**) PFM phase voltage hysteresis loop and (**e**) amplitude voltage butterfly loop.
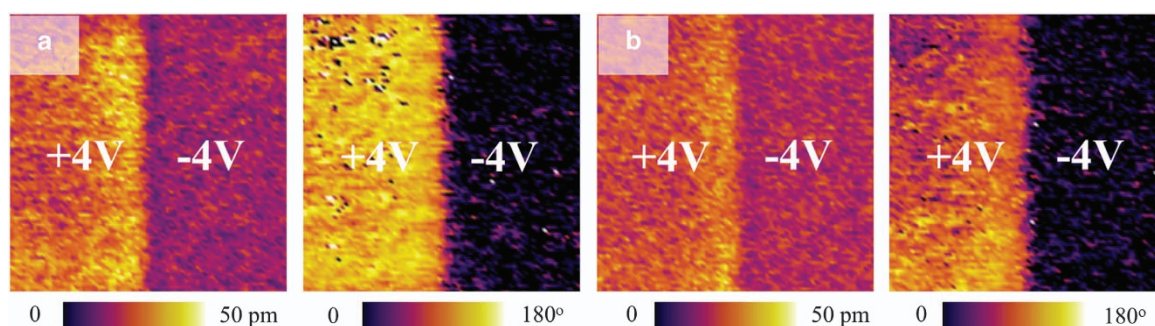

Figure 4. Piezoelectric force microscopy images (left: amplitude contrast; right: phase contrast) of polarisation domains for the epitaxial YMO film. The images were recorded after poling (**a**) 0 and (**b**) for 4 h by using poling bias of ±4 V in a $1.0 \times 1.0 \ \mu m^2$ area.

the good ferroelectricity and nearly complete polarisation switching behaviour.

To show the polarisation reversal and retention, the epitaxial YMO film was first electrically polarised by an external scanning electric field at a pre-designed area, in which the right half was polarised downwards by a negative electric bias of − 4 V, and the left half was polarised upwards with a positive bias of 4 V. Then, the vertical piezoresponse force microscopy measurement was performed immediately after the polarisation (Figure 4a, left: amplitude; right: phase) and 4 h after the polarisation (Figure 4b, left: amplitude; right: phase). The clear contrasts demonstrate the complete polarisation reversal upon the electrical polarisation process. The polarisation retention performance is also very good.

Nevertheless, the result of thin films is very different from the observation on bulk single-crystal samples. In this work, the vertical piezoresponse force microscopy characterisations on our thin-film samples failed to detect any vortex domain structure similar to that observed in bulk single crystals. One reason is that the vortex domain structure in thin films is much smaller than that

in bulk single crystals, which is a few micrometres or larger.[11,14,17] This may be due to the thin-film geometry or/and the strain induced by substrates. In order to check this possibility, we performed the in-plane TEM observation. Figure 5a shows a representative dark-field image of a fresh-state YMO film, which was taken along the [100] direction. By the comparison with the earlier observations, which were showing the bright and dark contrasts associated with the opposite polarisation domains, we can observe an intriguing feature: there are many local regions in which the bright and dark contrasts alternate around one centre point. The typical size for such regions is about 20 nm, smaller than the spatial resolution of the vertical piezoresponse force microscopy machine used in this study considering the fact that tip radius is typically ≈30 nm. The vortex domain pattern in the as-prepared YMO thin films is thus clearly identified although the vortex contrast is not as high as that in the bulk single crystals.

For better illustration of the vortex domain structure, a single vortex domain was enlarged and shown in the inset of Figure 5a. Clearly, the cloverleaf pattern may be assigned with a periodic
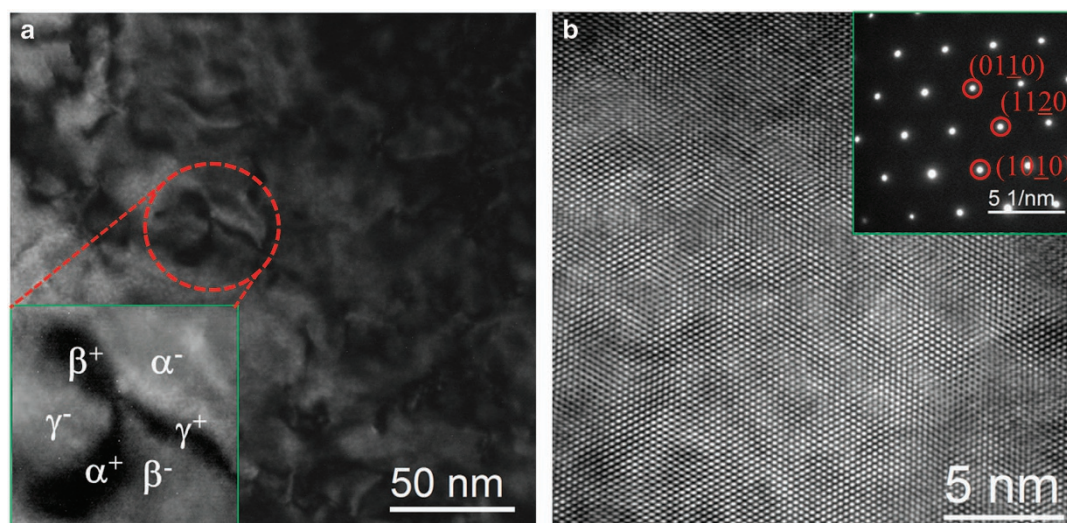
Figure 5. Plane-view HRTEM images of the epitaxial YMO film. (**a**) The dark-field TEM image in the [001] zone axis. The inset in (**a**) shows the enlarged single vortex domain with the domain configuration of $[\alpha^+, \gamma^-, \beta^+, \alpha^-, \gamma^+, \beta^-]$. (**b**) The corresponding HRTEM images of (**a**). The inset in (**b**) shows the diffraction spots in the observed region.

configuration of three types of antiphase domains surrounding the centre of the vortex core. This is consistent with the $[\alpha^+, \gamma^-, \beta^+, \alpha^-, \gamma^+, \beta^-]$ configuration identified in the bulk single crystals. In the HRTEM image shown in Figure 5b, the lattice dots are spatially uniform, indicating excellent crystal quality of the YMO film. A careful checking of the lattice space finds that the in-plane parameter a is ≈ 6.325 Å, which is consistent with the XRD results. The selected area electron diffraction in the explored region was also measured, as shown in the inset in Figure 5b, showing the sixfold symmetry characteristic of the (001)-oriented h-YMO film.

DISCUSSION

The vague contrast of the vortex domain structure in thin-film samples may be attributed to the shrinking of the out-of-plane lattice constant c, which leads to the reduced polarisation displacement. The small size (at nanoscale) of the domains may be related with the thin-film geometry and substrates. Following the similar strategy to the bulk single crystals, we also performed post-annealing of the samples at a temperature higher than T_c so that the vortex domain structure can be coarsened. However, a long-time annealing can damage the microstructural perfection of the Pt layer and the vortex pattern did not show significant coarsening. Furthermore, the vortex domains are sensitive to lattice defects such as dislocations or grain boundaries.[9] Such defects seriously affect the topological vortex structure. Overall, the cloverleaf domain patterns observed in the present YMO thin films are much clearer and remarkable than the earlier reported ones.[19] This work represents a significant progress towards the fabrication of vortex nano-domains and the control of vortex domains in h-YMO thin films. The result of this work will arouse promising application potentials in the development of new memory devices.

CONCLUSION

In summary, YMO film has been deposited successfully on the Pt-coated ALO(0001) substrate. XRD analysis characterised the epitaxial relationships with in-plane (0001)YMO/(111)Pt/(0001)ALO and out-of-plane [10$\bar{1}$0]YMO/(210)h-Pt/[10$\bar{1}$0])ALO. The cross-sectional HRTEM further proved the high-quality epitaxial properties of the heterostructure with very flat interfaces and surface.

Atomic force microscopy determined the epitaxial h-YMO film has a low roughness surface with root-mean-square roughness of 0.3 nm. Piezoresponse force microscopy revealed good polarisation reversible properties and stability of ferroelectric domains of the epitaxial h-YMO film. Especially, the dark-field HRTEM exhibited clearly vortex domains with size of ~ 20 nm, which constitutes a step towards the development of nano-size ferroelectric vortex domains in h-YMO film.

MATERIALS AND METHODS

To obtain the conducting bottom electrode with hexagonal in-plane symmetry prior the YMO growth, we deposited a Pt thin layer (~ 20 nm thickness) on each (ALO(0001)) substrate using pulsed laser deposition using a KrF excimer laser (248 nm wavelength) at an Ar ambient of 5×10^{-3} Pa and a substrate temperature of 450 °C. Next, the YMO films were grown on the Pt-coated ALO(0001) substrates. The films were deposited at a substrate temperature of 800 °C in an oxygen pressure of 0.7 Pa. At the end of the growth, the samples were kept in the oxygen ambient of 300 Pa while the substrates were maintained at 600 °C. The crystal structure and epitaxy of the Pt/ALO(0001) and YMO/Pt/ALO(0001) heterostructures were characterised by XRD using the Cu K_α radiation (PANalytical, Almelo, The Netherlands, PANalytical X9 Pert PRO). The cross-sectional TEM images were obtained from a HRTEM (JEOL, Akishima, Japan, JEOL 2011). The film surface topology was examined by atomic force microscopy. The ferroelectric domain structures were probed by piezo-response force microscopy (Asylum Research, Santa Barbara, CA, USA, Cypher) using a dual-frequency resonant-tracking technique. The vortex domains of YMO film were observed by plane-view dark-field TEM technique.

CONTRIBUTIONS

MZ supervised this project; HZP and FYZ performed the experiments; JYD performed the TEM testing; MZ, XSG and HZP analysed the data; MZ, HZP and QLL wrote the manuscript. The other authors commented on the manuscript.

COMPETING INTERESTS

The authors declare no conflict of interest.

REFERENCES

1. Dong, S., Liu, J.-M., Cheong, S.-W. & Ren, Z. F. Multiferroic materials and magnetoelectric physics: symmetry, entanglement, excitation, and topology. *Adv. Phys.* **64**, 519–626 (2015).
2. Ratcliff, W., Lynn, J. W., Kiryukhin, V., Prashant, J. & Fitzsimmons, M. R. Magnetic structures and dynamics of multiferroic systems obtained with neutron scattering. *npj Quantum Mater.* **1**, 16003 (2016).
3. Lee, S. *et al.* Giant magneto-elastic coupling in multiferroic hexagonal manganites. *Nature* **451**, 805–808 (2008).
4. Cho, D.-Y. *et al.* Ferroelectricity driven by Y d^0-ness with rehybridization in $YMnO_3$. *Phys. Rev. Lett.* **98**, 217601 (2007).
5. Aken, B. B. V., Palstra, T. T. M., Filippetti, A. & Spaldin, N. A. The origin of ferroelectricity in magnetoelectric $YMnO_3$. *Nat. Mater.* **3**, 164–170 (2004).
6. Artyukhin, S., Delaney, K. T., Spaldin, N. A. & Mostovoy, M. Landau theory of topological defects in multiferroic hexagonal manganites. *Nat. Mater.* **13**, 42–49 (2014).
7. Lin, S. Z. *et al.* Topological defects as relics of emergent continuous symmetry and Higgs condensation of disorder in ferroelectrics. *Nat. Phys.* **10**, 970 (2014).
8. Chae, S. C. *et al.* Self-organization, condensation, and annihilation of topological vortices and antivortices in a multiferroic. *Proc. Natl Acad. Sci. USA* **107**, 21366–21370 (2010).
9. Han, M. G. *et al.* Ferroelectric switching dynamics of topological vortex domains in a hexagonal manganite. *Adv. Mater.* **25**, 2415–2421 (2013).
10. Chae, S. C. *et al.* Evolution of the domain topology in a ferroelectric. *Phys. Rev. Lett.* **110**, 167601 (2013).
11. Choi, T *et al.* Insulating interlocked ferroelectric and structural antiphase domain walls in multiferroic $YMnO_3$. *Nat. Mater.* **9**, 253–258 (2010).
12. Geng, Y. *et al.* Direct visualization of magnetoelectric domains. *Nat. Mater.* **13**, 163–167 (2014).
13. Yu, Y. *et al.* Atomic-scale study of topological vortex-like domain pattern in multiferroic hexagonal manganites. *Appl. Phys. Lett.* **103**, 032901 (2013).
14. Zhang, Q. H. *et al.* Direct observation of multiferroic vortex domains in $YMnO_3$. *Sci. Rep.* **3**, 2741 (2013).
15. Du, Y. *et al.* Manipulation of domain wall mobility by oxygen vacancy ordering in multiferroic $YMnO_3$. *Phys. Chem. Chem. Phys.* **15**, 20010–20015 (2013).
16. Kumagai, Y. *et al.* Observation of persistent centrosymmetricity in the hexagonal manganite family. *Phys. Rev. B* **85**, 174422 (2012).
17. Wang, X. Y., Huang, F. T., Hu, R. W., Fan, F. & Cheong, S.-W. Self-poling with oxygen off-stoichiometry in ferroelectric hexagonal manganites. *APL Mater.* **3**, 041505 (2015).
18. Du, Y. *et al.* Domain wall conductivity in oxygen deficient multiferroic YMnO3 single crystals. *Appl. Phys. Lett.* **99**, 252107 (2011).
19. Kobayashi, K. *et al.* Real-space imaging of ferroelectric and structural antiphase domains in hexagonal $YMnO_3$. *J. Korean Phys. Soc.* **62**, 1077–1081 (2013).
20. Chen, Z. B., Wang, X. L., Ringer, S. P. & Liao, X. Z. Manipulation of nanoscale domain switching using an electron beam with omnidirectional electric field distribution. *Phys. Rev. Lett.* **117**, 027601 (2016).
21. Das, H., Wysocki, A. L., Geng, Y. N., Wu, W. D. & Fennie, C. J. Bulk magnetoelectricity in the hexagonal manganites and ferrites. *Nat. Commun.* **5**, 2998 (2014).
22. Kumagai, Y. & Spaldin, N. A. Structural domain walls in polar hexagonal manganites. *Nat. Commun.* **4**, 1540 (2013).
23. Mettout, B., Toledano, P., Lilienblum, M. & Fiebig, M. Combinatorial model for the ferroelectric domain-network formation in hexagonal manganites. *Phys. Rev. B* **89**, 024103 (2014).
24. Fang, Y. W. *et al.* First-principles studies of multiferroic and magnetoelectric materials. *Sci. Bull.* **60**, 156–181 (2015).
25. Martin, L. W., Chu, Y. H. & Ramesh, R. Advances in the growth and characterization of magnetic, ferroelectric, and multiferroic oxide thin films. *Mat. Sci. Eng. R* **68**, 89–226 (2010).
26. Fontcuberta, J. Multiferroic $RMnO_3$ thin films. *C. R. Physique* **16**, 204–226 (2015).
27. Zhang, R. L., Chen, C. L., Duan, M. M., Niu, L. W. & Jin, K. X. Piezoelectric, ferroelectric properties of multiferroic $YMnO_3$ epitaxial film studied by piezoresponse force microscopy. *J. Cryst. Growth* **390**, 56–60 (2014).
28. Ito, D., Fujimura, N., Yoshimura, T. & Ito, T. Ferroelectric properties of $YMnO_3$ epitaxial films for ferroelectric-gate field-effect transistors. *J. Appl. Phys.* **93**, 5563–5567 (2003).
29. Marti, X. *et al.* Epitaxial growth of biferroic $YMnO_3$(0 0 0 1) on platinum electrodes. *J. Cryst. Growth* **299**, 288–294 (2007).
30. Bachelet, R. *et al.* Enhanced thermal stability of Pt electrodes for flat epitaxial biferroic-$YMnO_3$/Pt heterostructures. *Appl. Phys. Lett.* **95**, 181907 (2009).